Supplementary Information for "Gravitational wave detectors with broadband high frequency sensitivity"

Michael A. Page[1, 2,*] Maxim Goryachev[3], Haixing Miao[4], Yanbei Chen[5], Yiqiu Ma[6], David Mason[7], Massimiliano Rossi[8, 9], Carl D. Blair[1], Li Ju[1], David G. Blair[1], Albert Schliesser[8, 9], Michael E. Tobar[3], and Chunnong Zhao[1]

[1]*Australian Research Council Centre of Excellence for Gravitational Wave Discovery, University of Western Australia, 35 Stirling Highway, Perth, Western Australia 6009, Australia*

[2]*Gravitational Waves Science Project, National Astronomical Observatory of Japan, 2-21-1 Osawa, Mitaka, 181-8588, Tokyo, Japan*

[3] *Australian Research Council Centre of Excellence for Engineered Quantum Systems, University of Western Australia, 35 Stirling Highway, Perth, Western Australia 6009, Australia*

[4] *Astrophysics and Space Research Group, University of Birmingham, Birmingham B15 2TT, United Kingdom*

[5] *Theoretical Astrophysics, California Institute of Technology, 1200 E California Blvd, Pasadena, California 91125, United States*

[6] *Center for Gravitational Experiment, School of Physics, Huazhong University of Science and Technology, Wuhan, 430074, China*

[7] *Yale Quantum Institute, Yale University, 17 Hillhouse Ave, New Haven, Connecticut 06511, United States*

[8] *Niels Bohr Institute, University of Copenhagen, Blegdamsvej 17, 2100 Copenhagen, Denmark and*

[9] *Denmark National Research Foundation Centre of Excellence for Hybrid Quantum Networks, University of Copenhagen, Blegdamsvej 17, 2100 Copenhagen, Denmark*

SUPPLEMENTARY NOTE 1 - BACKGROUND OF WHITE LIGHT SIGNAL RECYCLING (WLSR) REQUIREMENTS

The optomechanics of the negative dispersion filter can be characterised by a Hamiltonian given by:

$$\hat{H} = \hat{H}_{\rm opt} + \hat{H}_{\rm mech} + \hat{H}_{\rm int} + \hat{H}_{\rm ext}^{\rm opt} + \hat{H}_{\rm ext}^{\rm mech}. \tag{S1}$$

The interaction component is given by the following form:

$$\hat{H}_{\rm int} = -\hbar \frac{d\omega}{dq} x_{\rm zpf} (\hat{b} + \hat{b}^\dagger) \hat{a}^\dagger \hat{a}, \tag{S2}$$

where $\hat{a}$ and $\hat{b}$ are the annihilation operators of the optical and mechanical modes inside the cavity. The free Hamiltonians for the optical and mechanical resonances inside the filter cavity are denoted by $\hat{H}_{\rm opt}$ and $\hat{H}_{\rm mech}$. Langevin coupling to the external bath is denoted by $\hat{H}_{\rm ext}^{\rm opt}$ and $\hat{H}_{\rm ext}^{\rm mech}$ [1, 2]. The optical frequency shift per unit of generalised mechanical displacement is given by $d\omega/dq$ and $x_{\rm zpf}$ represents mechanical zero point fluctuations. The filter cavity operates by parametric interaction with gravitational wave (GW) signal fields at frequency $\omega_0 \pm \Omega$, where ω_0 is the interferometer carrier frequency and Ω the GW frequency. To mediate this interaction, the filter pump is blue detuned from the interferometer carrier by the mechanical resonance $\omega_{\rm m}$. In this scheme, the optomechanical coupling Hamiltonian can be expressed in a linearised form using the rotating wave approximation in the interaction picture, resulting in equation 1 of the main text.

After applying Heisenberg's equations of motion, transferring the differential equations to the frequency domain and removing small terms, the GW signal transfer function is found. GW sidebands acquire a frequency dependent negative phase that depends on the optomechanical anti-damping $\gamma_{\rm opt}$. By matching g to $\gamma_{\rm opt}$ and filter cavity bandwidth $\gamma_{\rm f}$ such that $\gamma_{\rm opt} = g^2/\gamma_{\rm f}$, the GW signal sideband transfer becomes [3]:

$$\hat{a}_{\rm out}(\omega_0 + \Omega) = \frac{\Omega + {\rm i}\gamma_{\rm opt}}{\Omega - {\rm i}\gamma_{\rm opt}} \hat{a}_{\rm in}(\omega_0 + \Omega) = {\rm e}^{-2{\rm i}\phi} \hat{a}_{\rm in}(\omega_0 + \Omega), \tag{S3}$$

where $\phi = \arctan\left(\Omega/\gamma_{\rm opt}\right)$. The optomechanical coupling can be tuned such that the negative dispersion phase ϕ matches the GW signal sideband phase delay $\Omega L_{\rm arm}/c$ acquired from travel inside the interferometer arm cavity of length $L_{\rm arm}$, which implies

* Corresponding author:mpagephys@gmail.com

$\gamma_{\rm opt} = c/L_{\rm arm}$. For example, a 4 km long GW detector requires $\gamma_{\rm opt}/(2\pi) = 12$ kHz. The linear negative dispersion regime $\phi \sim \Omega/\gamma_{\rm opt}$ applies for $\Omega \ll \gamma_{\rm opt}$, where the transfer function can be simplified to equation 2 shown in the main text.

Extra vacuum noise sidebands are present at $\omega_0 + 2\omega_{\rm m} \pm \Omega$ as shown in figure 6 of the main text Methods. These interact to produce extra noise at the gravitational wave sideband frequency. Solving for the transfer function of a detuned cavity, it is possible to show that the noise sidebands around $\omega_0 + 2\omega_{\rm m}$ have a first order contribution proportional to $\gamma_{\rm f}/\omega_{\rm m}$, such that:

$$\begin{aligned}\hat{a}_{\rm out}(\omega_0+\Omega) =& e^{-2i\phi}\hat{a}_{\rm in}(\omega_0+\Omega) \\ &- \frac{\gamma_{\rm f}}{\omega_{\rm m}}\frac{\gamma_{\rm opt}}{\Omega - i\gamma_{\rm opt}}\hat{a}(\omega_0+2\omega_{\rm m}-\Omega),\end{aligned} \tag{S4}$$

where in this case the noise sideband at frequency $\omega_0 + 2\omega_{\rm m} - \Omega$ contributes noise to GWs at frequency $\omega_0 + \Omega$. The extra noise sidebands of the detuned cavity introduce imperfect phase cancellation, reducing potential bandwidth enhancement from WLSR. Previous schemes for WLSR interferometry in GW detectors used pendulum resonators with $\omega_{\rm m}/(2\pi) < 200$ kHz [4, 5]. The low mechanical frequency places strict requirements on the filter cavity finesse to reduce coupling of $\omega_0 + 2\omega_{\rm m} \pm \Omega$ noise sidebands to the GW signal. However, the high finesse filter cavity also increases the fractional contribution of filter cavity round trip optical loss $\epsilon_{\rm f}$. The higher mechanical frequency of the resonators described in this paper allows significant suppression of sideband noise even for high bandwidth filters, which makes the optical cavity design requirements much more flexible.

The use of an optomechanical resonator in the filter cavity introduces thermal noise into the main interferometer, which must be minimised in order to maintain integrity of the sensitivity. The expectation value of the thermal bath operator is $\langle \hat{b}^\dagger_{\rm th}\hat{b}_{\rm th}\rangle \sim k_{\rm B}T(\hbar\omega_{\rm m})^{-1}$ inside the filter, where $k_{\rm B}$ represents Boltzmann's constant. The temperature T and quality factor $Q_{\rm m}$ requirement can be derived from the equations of motion for the mechanical mode in the filter, [3]:

$$\frac{T}{Q_{\rm m}} < \frac{\hbar\gamma_{\rm ifo}}{8k_{\rm B}}, \tag{S5}$$

where $\gamma_{\rm ifo}$ is a characteristic bandwidth that depends on the detector configuration. For example, in an Advanced LIGO type interferometer we must use a phononic crystal (PNC) resonator with a Q-factor of 1.03×10^9 operating near 1 K temperature.

SUPPLEMENTARY NOTE 2 - MECHANICAL LOSS OF BULK ACOUSTIC WAVE (BAW) RESONATORS

In this section we detail the mechanical loss of BAW resonators at low temperature. In the event that the issues with low optomechanical coupling can be overcome, their low thermal noise is promising for broadband GW detectors.

A BAW resonator may be regarded as the phononic analogue of an optical Fabry-Perot cavity. Typically they are made of a thin plate of a dielectric material which supports phonons of shear and longitudinal polarisations. Acoustic waves are reflected by the interface between vacuum and crystal, thus the thickness of the crystal sets the resonance conditions for different overtone modes.

BAW resonators have been shown to achieve extremely high $Q_{\rm m} > 10^9$ at hundreds of MHz and cryogenic temperatures. For long-lived phonons at low temperature, internal mechanical loss of BAW resonators is dominated by crystal lattice anharmonicity in the Landau-Rumer regime where the mechanical quality factor is inversely proportional to temperature and independent of frequency [6]. The power law scaling of $Q_{\rm m}$ with temperature has been experimentally demonstrated to be $Q_{\rm m} \sim T^{-6.5}$ for quartz BAW resonators at liquid helium temperatures of 3–20 K [7, 8].

The optimal longitudinal mode number is dictated by the compromise between clamping loss and surface scattering loss. Energy leakage through the resonator support is a primary source of mechanical loss at low mode number. To overcome this effect in BAW devices, the crystal is designed with a plano-convex lens shape. The radius of curvature of the convex face creates a potential well that traps phonons in the central part of the disk. The corresponding distribution of acoustic energy has a Gaussian-like profile, thus reducing the energy loss into the support [9]. Higher overtone modes typically result in better phonon trapping, since the mode amplitude at the edge of the crystal is smaller [10]. However, at high overtone numbers frequency dependent scattering loss becomes dominant. Surface roughness scattering comes from imperfections on the surface layer of the crystal. The loss contribution increases as the acoustic wavelength approaches the imperfection size. Surface scattering has been found to scale with longitudinal mode number m as $Q_{\rm scattering} = \frac{2}{m}\cdot 10^{12}$ for quartz resonators. The optimal mode to balance support and scattering losses is found to have $m = 65$, $\omega_{\rm m}/(2\pi) = 204$ MHz, with $Q_{\rm m} = 8 \times 10^9$ at 4 K. To achieve improved Q-factor at higher mode number, one would need to suppress the standard deviation of the the surface roughness to a level better than 1-4 nm.

At temperatures of less than 1 K, the dominant temperature-scaling loss switches from the Landau-Rumer regime to intrinsic Two Level System (TLS) loss caused by impurities. Premium grade quartz crystals typically contain impurity ions such as

Al^{3+}, Na^{+}, Si^{4+}, etc. at a concentration of a few parts per billion. TLS-limited Q-factor dependence on temperature is typically $Q_{TLS} \sim T^{-0.3}$ for quartz crystals [7, 8], which is supported by additional observations such as power dependence of losses, strong non-Duffing nonlinearities [11] and magnetic field sensitivity [12]. Comparison of experimental results with TLS theory gives a projected quality factor of the optimal BAW resonator mode shown in figure S1 [8]. Extrapolating the TLS limited Q-factor reveals a limit of $Q_m = 1.5 \times 10^{10}$ at 1 K temperature, which is used to produce the curve "BAW Ultra-low loss" in figure 1 of the main text. The extrapolated thermal noise value represents a factor of 7.5 improvement in thermal noise coupling from the filter cavity to the interferometer, and a $\sqrt{7.5}$ improvement in the thermal noise contribution to the total strain sensitivity amplitude. The ultra low-loss 4 km WLSR interferometer is capable of reaching $h < 5 \times 10^{-25}$ $Hz^{1/2}$ in the 1–5 kHz band.

Most sources of frequency noise for BAW resonators are significantly reduced in a typical cryogenic environment, leaving only the temperature fluctuations and external vibration as the prevailing factors [13, 14]. Reduction of vibration sensitivity requires a stress compensated cut and crystal orientation with respect to main mode of vibration of the cryocooler [14]. Due to high degree of isolation of the acoustic wave from the environment and high operating frequencies, vibration from external sources has not been observed on any thermal noise spectra.

SUPPLEMENTARY NOTE 3 - ABSORPTION HEATING OF MECHANICAL RESONATORS

Heating of the resonators used in the negative dispersion filter may be a concern. In the case of the PNC it is due to the thermal resistance of the geometry, namely the thinness of the resonator and phononic shield. In the case of the quartz BAW resonator it is due to the high laser power incident on the surface that is necessitated by the filter cavity pumping requirement.

Measured low temperature mechanical properties of a silicon nitride PNC resonator under optical illumination are shown in figure S2. It is seen that it is possible to maintain the temperature of a the sample close to 5 K for a few mW of incident laser power. Note that the sample in question differs from that referred to throughout this paper, in that the resonator is 60 nm thick rather than 20 nm thick, and ~ 800 nm laser light was used, which has slightly higher optical absorption in Si_3N_4 compared to 1064 nm light used in our WLSR design. Thin resonators are required for higher quality factors, and also have less optical absorption. However, thicker resonators also have less thermal resistance.

Silicon nitride membranes have been shown to have low optical absorption of near-infrared light. Wilson has suggested an upper limit to the refractive index imaginary component of $\mathrm{Im}(n_{SiN}) \leq 0.8 \times 10^{-5}$, corresponding to a power absorption of $\lesssim 4.5$ ppm for a 20 nm thick membrane [15]. Sankey *et al.* report even lower absorption of $\mathrm{Im}(n_{SiN}) \leq 1.5 \times 10^{-6}$ for Si_3N_4 with 1064 nm light [16]. In addition, Peterson *et al.* measured optomechanical damping of the motion of a 40 nm thick Si_3N_4 membrane resonator, and suggested that material absorption was not a dominant contributor to the bath temperature of 360 mK, even with input power of 5 μW into a cavity with finesse 57,000 [17]. These measurements of low absorption with membrane resonators are encouraging, however, due to the nature of manufacturing microresonators, we emphasise that the projections of absorption heating are meant as a guide only.

For the BAW resonator, a 1-dimensional order of magnitude estimate of resonator heating is obtained using the following conduction law:

$$P_{\mathrm{conduct}} = P_{\mathrm{absorb}} = -\sigma\kappa(T)\frac{dT(z)}{dz} \tag{S6}$$

where P_{conduct} is the power conducted through a channel of cross sectional area σ and length dimension z in the direction of heat conduction. P_{conduct} is assumed to be equal to the absorbed optical power P_{absorb}. Assuming that, at cryogenic temperatures, the thermal conductivity can be approximated by a constant times temperature to a constant power, i.e. $\kappa = \kappa_0 T^n$, and integrating with respect to z gives:

$$T_{\mathrm{equilib}} = \left(\frac{P_{\mathrm{absorb}}(n+1)l_{\mathrm{lim}}}{\kappa_0\sigma} + T_{\mathrm{external}}^{n+1}\right)^{1/(n+1)} \tag{S7}$$

where l_{lim} is the length of the limiting component of thermal resistivity, T_{external} is the temperature of cryogenics for which we nominally maintain the resonator, and T_{equilib} is the equilibrium temperature of the resonator assuming that heat can escape via conduction. For the BAW resonator we look at conduction through a channel with length of $l_{\mathrm{lim}} = 15$ mm and cross sectional area $\sigma = 5$ mm^2 which is approximately based on contact area of the clamps shown in the publication of Galliou *et al.* demonstrating $Q_m = 8 \times 10^9$ in BAW resonators [8]. External cryogenics are maintained at 4 K. The cryogenic temperature dependent thermal conductivity for quartz is obtained from values measured by Hofacker and Lohneysen [18] and below 5 K is approximately equal to $\kappa \sim 10\ T^{2.5}$.

The equilibrium temperatures of the BAW resonator is shown in figure S3 for three different values of optical absorption. In the approximation of 1-dimensional conduction, maintaining the resonator at less than 1 K temperature difference from the

environment is plausible, but would require optical absorption of less than 5 ppm. Fused quartz used in GW detector optics has an absorption coefficient of less than 1 ppm cm^{-1} at 1064 nm due to high purity [19], which contributes to its extremely high damage threshold.

SUPPLEMENTARY NOTE 4 - NEGATIVE DISPERSION OPTOMECHANICS WITH BULK ACOUSTIC WAVE RESONATORS

In the main text, we demonstrated the possibility of creating WLSR using a PNC membrane resonator that interacts with light using the established method of membrane-in-the-middle optomechanics. The possibility of using millimeter-scale BAW resonators was also mentioned due to their appealing thermal noise properties, but there are outstanding issues with achieving the desired level of optomechanical coupling while maintaining a sufficient mechanical quality factor. Here we elaborate on the background and issues with optomechanical coupling of BAW resonators, in the context of WLSR GW detectors.

Optomechanical coupling to the antiphase surface motion of a quartz resonator is relatively small. Even with a high finesse cavity of input transmission 100 ppm, for a cavity length of 50 mm, circulating power of 38 kW is required. This extreme power requirement is part of the motivation for exploring WLSR using less $\gamma_{\rm opt}/(2\pi) \sim 1000$ Hz in exchange for a slightly reduced bandwidth of sensitivity enhancement. The relationship of filter cavity power $P_{\rm f}$ versus filter cavity length $L_{\rm f}$ is shown in figure S4, using $\gamma_{\rm opt}/(2\pi) = 900$ Hz specifically chosen for this alternate filter design. It is seen that $L_{\rm f} < 10$ mm greatly increases the requirement on $P_{\rm f}$. Decreasing the filter cavity input transmission $T_{\rm f}$ is seen to decrease the required filter cavity power, and as per equation S4 also decreases the contribution of quantum noise from $\omega_0 + 2\omega_{\rm m} \pm \Omega$ sidebands. However, the fundamental bandwidth broadening effect of WLSR scales with with $\gamma_{\rm f}$ [20], and $T_{\rm f}$ in the range 100–1000 ppm is chosen to balance these factors. Choosing $T_{\rm f} = 100$ ppm gives a power requirement of approximately 2.5 kW, resulting in a beam intensity of 1.2 MW/cm^2. The damage threshold of quartz with respect to near-infrared light is reportedly greater than 1 GW/cm^2 [21, 22]. However, it remains to be seen whether or not the power and intensity levels can be sustained in a cryogenic high-Q resonator. Possible issues may include wavefront distortion and loss from heat gradients.

Increasing the reflectivity of the crystal by changing the refractive index is one possible means to increase the optomechanical coupling and reduce the filter cavity circulating power as per equation 3 of the main text. The dependence of the optomechanical frequency shift versus BAW resonator refractive index is shown in figure S5. Coating the surface of the BAW resonator with one quarter wave layer of dielectric can further enhance the reflectivity and optomechanical coupling. For example, using a quarter wave layer of silicon nitride on both sides of the resonator raises the effective refractive index of the crystal to 2.54. Given the thickness ratio of coating to substrate (hundreds of nm versus 1 mm), there is a possibility that the mechanical Q-factor will not be degraded too much by the surface treatment, but this bears more detailed investigation in future work.

It may be possible to design a BAW resonator that can support Brillouin scattering interactions at a high mechanical quality factor. We also note that future GW detectors may use wavelength $\lambda = 2\ \mu$m optics, which would reduce the BAW resonator's Brillouin scattering frequency by half. This is important for reducing the effect of surface scattering losses that limit the mechanical Q-factor of longitudinal bulk acoustic mechanical modes in the GHz frequencies. These considerations will be useful for the possibility of designing custom BAW resonators for GW detector optomechanics.

SUPPLEMENTARY NOTE 5 - REDUCING THE POWER REQUIREMENT FOR OPTOMECHANICAL COUPLING

WLSR configurations can be made to use less optomechanical coupling $\gamma_{\rm opt}$, and thus less filter cavity power, at the expense of slightly lower bandwidth enhancement. This idea is useful for reducing the extremely large filter cavity power requirement of BAW resonators. The required layout is shown in figure S6. The interferometer uses the dual-recycling Fabry-Perot Michelson configuration. Unlike the signal extraction mirror (SEM) in figure 1 of the main text, the SEM here is not perfectly impedance matched to the arms. Instead, the input test mass (ITM) and SEM are configured such that they form a compound mirror with effective arm cavity bandwidth of $\gamma_{\rm arm}/(2\pi) = 1$ kHz [23]. This can be achieved with ITM and SEM transmissivities $T_{\rm ITM} = 0.033$ and $T_{\rm SEM} = 0.33$.

The result of WLSR using reduced $\gamma_{\rm opt}$ is shown in figure S7. These are compared to the WLSR curves using $\gamma_{\rm opt}/(2\pi) = 12$ kHz applied to the configuration of figure 1 of the main text. However, the WLSR curves of figure S7 use 800 kW arm cavity power, zero squeezed vacuum input and interferometer optical losses are comparable to the target loss of the A+ upgrade to Advanced LIGO [24]. Filter cavity round trip losses are maintained near 20 ppm in order to bring their respective optical loss close to the quantum noise level at 1–5 kHz. Full noise budgets for the curves shown in figure S7 are detailed in the following section and table S2.

SUPPLEMENTARY NOTE 6 - NOISE CONTRIBUTIONS TO WLSR INTERFEROMETERS

Here we elaborate on further findings from the WLSR interferometer design framework outlined in the main text and Methods.

The WLSR sensitivity curves shown in figure 1 of the main text use a configuration loosely based on future GW detectors such as Einstein Telescope. The key features of these detectors with respect to this paper are the application of 10 dB frequency dependent squeezing to reduce quantum noise across the entire GW band, arm cavity power of several MW, improved thermal compensation of test mass distortion, reduced Brownian noise of test mass optical coatings and extremely low optical losses in the interferometer. Interferometer test mass coating thermal noise is unlikely to be a significant contributor in the high frequency band of interest. Relevant parameters used in the calculation of figure 1 of the main text are shown in table 1 of the main text and table S1.

A breakdown of the noise sources for the key results of figure 1 in the main text are shown in figure S8. As mentioned in the main text Results, the limiting noise sources for this particular interferometer configuration are filter cavity thermal noise and optical losses from the filter cavity and interferometer beamsplitter cavity. The combined arm cavity and SRC loss is set to 0.12%, which is below the limiting noise sources in the 1–5 kHz band, and close to the BAW resonator thermal noise contribution in the 100-2000 Hz band.

A high-frequency detector scheme using Advanced LIGO-style dual recycling topology was analysed by Martynov *et al.* [25], which exploits optical sloshing between the arm cavity and signal recycling cavity (SRC). The optical resonance and bandwidth of the sloshing interaction between the arm cavity and SRC is mediated by transmissivities $T_{\rm ITM}$, $T_{\rm SR}$ and cavity lengths $L_{\rm arm}$, $L_{\rm SRC}$ of the arm cavity and SRC. Tuning the signal recycling parameters allows for the sloshing interaction to resonantly enhance signals in the neutron star frequency band. A comparison of a dual recycling sloshing interferometer scheme with low-loss WLSR is shown in figure 1 of the main text. The noise curve for the sloshing interferometer accounts for quantum noise as well as resonantly enhanced thermal lensing in the beamsplitter cavity. The "sloshing SR", "PNC" and "BAW" curves use identical thermal lensing compensation parameters shown in the "PNC" column of table S1. It can be seen that WLSR is capable of achieving better sensitivity over a broader band of neutron star frequencies, given the same level of squeezing, arm length and thermal lensing compensation. The WLSR curve shown in figure 1 of the main text also additionally accounts for arm/SRC optical losses, whereas the sloshing SRC curve in the same figure disregards arm/SRC losses and thus its relative sensitivity is slightly overestimated.

The WLSR sensitivity curves shown in figure S7 use a configuration loosely based on current and near-future GW detectors such as Advanced LIGO and A+. The arm cavity maintains 800 kW of optical power, no frequency dependent squeezing is applied, and interferometer optical losses are approximately 1%. Relevant parameters used in the calculation of figure S7 are shown in table S2.

A breakdown of noise sources for the set of WLSR interferometers in figure S7 is shown in figure S9. Loss parameters are shown in the relevant columns of table S2 corresponding to the type of resonator and optomechanical anti-damping value. The WLSR interferometer with the BAW resonator and $\gamma_{\rm opt}/(2\pi) = 12$ kHz achieves sensitivity of approximately 1.5×10^{-24} Hz$^{-1/2}$ for frequencies from 150 Hz to 4 kHz. For the case of the PNC, the resulting sensitivity is limited by thermal noise from the resonator. Arm/SRC optical losses at the level of 1% are comparable to the quantum noise floor. For both the PNC and BAW resonators, the filter cavity optical loss is significant in the band 1–5 kHz. This is due to the fact that the finesse of the filter cavity must be high to reduce the circulating power required, but this increases the fractional optical loss. In addition, the cases with lower $\gamma_{\rm opt}$ also display high filter cavity optical loss in the 1–5 kHz band. This is because the leading coefficient of noise terms in the filter cavity Heisenberg equations of motion have $\gamma_{\rm opt} - i\Omega$ in the denominator, causing their effects to become significant as $\Omega \to \gamma_{\rm opt}$.

SUPPLEMENTARY NOTE 7 - WLSR VERSUS DETECTOR ARM LENGTH AND ARM CAVITY POWER

The sensitivity of WLSR interferometers versus arm length are shown in figure S10, with parameters given in table S1. The negative dispersion effect is approximately linear for $\Omega \ll \gamma_{\rm opt}$, as per equation S3 - since the required $\gamma_{\rm opt}$ is inversely dependent upon arm length, longer interferometers begin to exhibit non-linear filter cavity phase at lower Ω. Longer interferometers also have a stricter thermal noise requirement from the filter cavity. However, their optical loss level is lower relative to the quantum noise floor. In particular, the filter cavity optical loss can be reduced by increasing the filter cavity bandwidth, which reduces its fractional loss contribution. The filter cavity power requirement decreases with arm length, allowing the filter bandwidth to be increased to meet a set pumping power target. Alternately, simply operating at a lower filter cavity pumping power is particularly useful with respect to the BAW resonator technology. It is seen that the 10 km WLSR interferometer can maintain superior sensitivity to a 4 km interferometers up to a frequency of 5 kHz, even given higher levels of $\epsilon_{\rm arm}$ and $\epsilon_{\rm f}$ as per table S1 and figure S10. The reduced power requirement versus interferometer length allows us greater flexibility in WLSR design, and as such the technology will be useful for long-arm future GW detectors such as Einstein Telescope and Cosmic Explorer.

We briefly compare our results across different levels of arm cavity power. In Table S2 a set of parameters is shown regarding an interferometer using 200 kW of arm cavity power, which is approximately the current level that has been achieved in Advanced LIGO [26]. Figure S11 shows a comparison of three different WLSR configurations - one using 200 kW arm power, one using 800 kW arm power and one using 4 MW arm power with 10 dB frequency dependent squeezing. It is seen that the 200 kW WLSR interferometer can reach a peak sensitivity comparable to that of the nominal Advanced LIGO design at 800 kW arm

power, but with bandwidth that extends to the neutron star frequencies at 1–5 kHz.

SUPPLEMENTARY REFERENCES

[1] C. W. Gardiner and M. J. Collett, "Input and output in damped quantum systems: Quantum stochastic differential equations and the master equation," Physical Review A **31**, 3761–3774 (1985).

[2] Yanbei Chen, "Macroscopic quantum mechanics: Theory and experimental concepts of optomechanics," Journal of Physics B: Atomic, Molecular and Optical Physics **46**, 104001 (2013).

[3] Haixing Miao, Yiqiu Ma, Chunnong Zhao, and Yanbei Chen, "Enhancing the bandwidth of gravitational-wave detectors with unstable optomechanical filters," Physical Review Letters **115**, 211104 (2015).

[4] Haixing Miao, Huan Yang, and Denis Martynov, "Towards the design of gravitational-wave detectors for probing neutron-star physics," Physical Review D **98**, 044044 (2018).

[5] Michael Page, Jiayi Qin, James La Fontaine, Chunnong Zhao, Li Ju, and David Blair, "Enhanced detection of high frequency gravitational waves using optically diluted optomechanical filters," Physical Review D **97**, 124060 (2018).

[6] L. Landau and G. Rumer, "Uber schall absorption in festen Körpen," Physikalische Zeitschrift der Sowjetunion **11**, 18–25 (1937).

[7] Maxim Goryachev, Daniel L. Creedon, Serge Galliou, and Michael E. Tobar, "Observation of Rayleigh phonon scattering through excitation of extremely high overtones in low-loss cryogenic acoustic cavities for hybrid quantum systems," Physical Review Letters **111**, 085502 (2013).

[8] Serge Galliou, Maxim Goryachev, Roger Bourquin, Philippe Abbé, Jean Pierre Aubry, and Michael E. Tobar, "Extremely low loss phonon-trapping cryogenic acoustic cavities for future physical experiments," Scientific Reports **3**, 2132 (2013).

[9] D. S. Stevens and H. F. Tiersten, "An analysis of doubly rotated quartz resonators utilizing essentially thickness modes with transverse variation," The Journal of the Acoustical Society of America **79**, 1811–1826 (1986).

[10] Maxim Goryachev and Michael E. Tobar, "Effects of geometry on quantum fluctuations of phonon-trapping acoustic cavities," New Journal of Physics **16**, 083007 (2014).

[11] M. Goryachev, W.G. Farr, Eu.N. Ivanov, and M.E. Tobar, "Anomalously strong nonlinearity of unswept quartz acoustic cavities at liquid helium temperatures," Journal of Applied Physics **114**, 094506 (2013).

[12] Maxim Goryachev, Serge Galliou, and Michael E. Tobar, "Observation of low-temperature magnetomechanic effects in crystalline resonant phonon cavities," Physical Review B **100**, 174108 (2019).

[13] Maxim Goryachev, Serge Galliou, Jol Imbaud, Roger Bourquin, Bernard Dulmet, and Philippe Abbe, "Recent investigations on BAW resonators at cryogenic temperatures," in *2011 Joint Conference of the IEEE International Frequency Control and the European Frequency and Time Forum (FCS) Proceedings* (2011) pp. 1–6.

[14] M. Goryachev, S. Galliou, Ph. Abbe, P.-Y. Bourgeouis, S. Grop, and B. Dubois, "Quartz resonator instabilities under cryogenic conditions," IEEE Transactions on Ultrasonics, Ferroelectrics, and Frequency Control **59**, 12494210 (2012).

[15] Dalziel J. Wilson, *Cavity Optomechanics with High-Stress Silicon Nitride Films*, Ph.D. thesis, California Institute of Technology (2012).

[16] J.C. Sankey, C. Yang, B.M. Zwickl, A.M. Jayich, and J.G.E Harris, "Strong and tunable nonlinear optomechanical coupling in a low-loss system," Nature Physics **6**, 707–712 (2010).

[17] R. W. Peterson, T. P. Purdy, N. S. Kampel, R. W. Andrews, P.-L. Yu, K. W. Lehnert, and C. A. Regal, "Laser cooling of a micromechanical membrane to the quantum backaction limit," Physical Review Letters **116**, 063601 (2016).

[18] M. Hofacker and H.v. Lohneysen, "Low temperature thermal properties of crystalline quartz after electron irradiation," Zeitschrift fur Physik B Condensed Matter **42**, 291–296 (1981).

[19] Vincent Loriette and Claude Boccara, "Absorption of low-loss optical materials measured at 1064 nm by a position-modulated collinear photothermal detection technique," Applied Optics **42**, 649–656 (2003).

[20] Joe Bentley, Philip Jones, Denis Martynov, Andreas Freise, and Haixing Miao, "Converting the signal-recycling cavity into an unstable optomechanical filter to enhance the detection bandwidth of gravitational-wave detectors," Physical Review D **99**, 102001 (2019).

[21] Xun Gao, Qi Li, Haijun Chi, and Jingquan Lin, "355nm and 1064nm laser damage of quartz glass," in *Third International Symposium on Laser Interaction with Matter*, Vol. 9543 (SPIE, 2015) pp. 124 – 128.

[22] A.A. Said, T. Xia, A. Dogariu, D.J. Hagan, M.J. Soileau, E.W. Van Stryland, and M. Mohebi, "Measurement of the optical damage threshold in fused quartz," Applied Optics **34**, 3374–3376 (1995).

[23] Alessandra Buonanno and Yanbei Chen, "Scaling law in signal recycled laser-interferometer gravitational-wave detectors," Physical Review D **67**, 062002 (2003).

[24] B. Lantz, S. Reid, R. Bassiri, G. Vajente, G. Hammond, S. Hild, Danilishin S., and V. Quetschke, *Instrument Science White Paper 2019*, Tech. Rep. LIGO-T1900409-v5 (LIGO Scientific Collaboration, 2019).

[25] Denis Martynov, Haixing Miao, Huan Yang, Francisco Hernandez Vivanco, Eric Thrane, Rory Smith, Paul Lasky, William E. East, Rana Adhikari, Andreas Bauswein, Aidan Brooks, Yanbei Chen, Thomas Corbitt, Andreas Freise, Hartmut Grote, Yuri Levin, Chunnong Zhao, and Alberto Vecchio, "Exploring the sensitivity of gravitational wave detectors to neutron star physics," Physical Review D **99**, 102004 (2019).

[26] A. Buikema *et al.*, "Sensitivity and performance of the Advanced LIGO detectors in the third observing run," Physical Review D **102**, 062003 (2020).

[27] J Aasi *et al.*, "Advanced LIGO," Classical and Quantum Gravity **32**, 074001 (2015).

Parameter	PNC	BAW	BAW ULL	PNC 2 km	PNC 10 km
Interferometer					
Circulating arm power P (MW)	4.0	4.0	4.0	4.0	4.0
Arm length $L_{\rm arm}$ (km)	4.0	4.0	4.0	2.0	10.0
Observed squeezing (dB)	10	10	10	10	10
Signal recycling mirror transmission $T_{\rm SR}$	0.025	0.025	0.01	0.01	0.1
Input test mass transmission $T_{\rm itm}$	0.04	0.04	0.04	0.04	0.04
Output to photodiode loss	0.025	0.025	0.01	0.025	0.025
Total arm losses $\epsilon_{\rm arm}$ (ppm)	1200	1200	800	850	3000
Input test mass thermal compensation $\kappa_{\rm ITM}$	70	70	90	70	70
Beamsplitter thermal comp. $\kappa_{\rm BS}$	10	10	10	10	10
Input test mass absorption $\alpha_{\rm ITM}$ (ppm)	0.25	0.25	0.25	0.25	0.25
Beamsplitter absorption $\alpha_{\rm BS}$ (ppm)	1.0	1.0	0.5	1.0	1.0
Signal extraction losses $\epsilon_{\rm se}$ (ppm)	957	957	500	957	957
Filter cavity					
Optomechanical anti-damping $\gamma_{\rm opt}/2\pi$ (kHz)	11.5	11.5	11.5	23.4	4.34
Filter cavity roundtrip loss $\epsilon_{\rm f}$ (ppm)	10	5	5	10	25
Filter cavity transmission $T_{\rm f}$ (ppm)	300	100	500	200	750
Filter cavity length $L_{\rm f}$ (m)	0.05	0.05	0.05	0.05	0.05
Thermal noise coupling $T/Q_{\rm m}$ (K)	1×10^{-9}	5×10^{-10}	6.5×10^{-11}	1×10^{-9}	1×10^{-9}

TABLE S1. **Properties of white light signal recycling (WLSR) schemes based on future gravitational wave detectors:** Certain white light signal recycling schemes in this paper are based around future detectors that use several MW of arm cavity circulating power, 10 dB frequency dependent squeezing of quantum noise and extremely low levels of optical loss. The first 3 columns refer to the key WLSR results in figure 1 of the main text, for both the phononic crystal (PNC) and bulk acoustic wave (BAW) resonators. Figure S10 shows WLSR with different interferometer lengths, the properties of which are denoted in the latter two columns.

Parameter	PNC 1.2 kHz	BAW 0.9 kHz	PNC 12 kHz	BAW 12 kHz	PNC 200 kW
Interferometer					
Circulating arm power P (MW)	0.80	0.80	0.80	0.80	0.20
Arm length $L_{\rm arm}$ (km)	4.0	4.0	4.0	4.0	4.0
Observed squeezing (dB)	0	0	0	0	0
Signal recycling mirror transmission $T_{\rm SR}$	0.2	0.1	0.01	0.01	0.01
Input test mass transmission $T_{\rm itm}$	0.033	0.033	0.033	0.033	0.033
Output to photodiode loss	0.05	0.05	0.05	0.05	0.05
Total arm losses $\epsilon_{\rm arm}$ (ppm)	12400	7400	7400	7400	9400
Input test mass thermal compensation $\kappa_{\rm ITM}$	30	30	60	60	30
Beamsplitter thermal comp. $\kappa_{\rm BS}$	1	1	2.5	2.5	1
Input test mass absorption $\alpha_{\rm ITM}$ (ppm)	0.5	0.5	0.5	0.5	0.5
Beamsplitter absorption $\alpha_{\rm BS}$ (ppm)	1.0	1.0	1.0	1.0	1.0
Signal extraction losses $\epsilon_{\rm se}$ (ppm)	1250	1250	257	257	78
Filter cavity					
Optomechanical anti-damping $\gamma_{\rm opt}/2\pi$ (kHz)	1.20	0.90	11.5	11.5	11.5
Filter cavity roundtrip loss $\epsilon_{\rm f}$ (ppm)	20	15	20	15	40
Filter cavity transmission $T_{\rm f}$ (ppm)	250	300	250	150	400
Filter cavity length $L_{\rm f}$ (m)	0.05	0.05	0.05	0.05	0.05
Thermal noise coupling $T/Q_{\rm m}$ (K)	3×10^{-9}	5×10^{-10}	3×10^{-9}	5×10^{-10}	4×10^{-9}

TABLE S2. **Properties of white light signal recycling (WLSR) schemes based on current and near-future gravitational wave detectors:** Certain WLSR schemes in this paper are based around current detectors that are designed for less than 1 MW of arm cavity circulating power. The first four columns are used for the key curves in figure S7, which compares WLSR schemes that use different levels of optomechanical anti-damping and filter cavity power for both the phononic crystal (PNC) and bulk acoustic wave (BAW) resonators. Also shown are the parameters for a configuration using 200 kW arm cavity power, seen in figure S11. The temperature of the PNC resonator in these configurations is raised compared to those detailed in table S1.

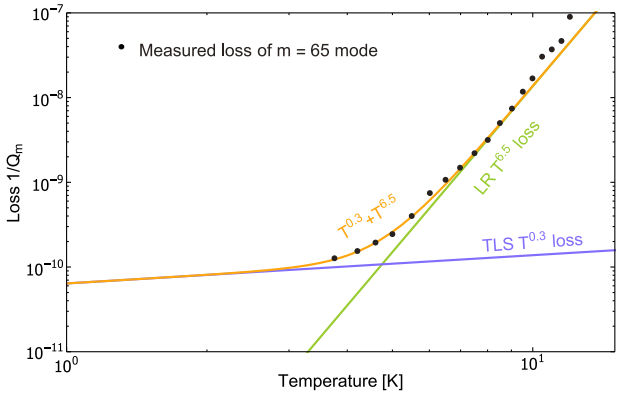

FIG. S1. **Mechanical loss of quartz bulk acoustic wave (BAW) resonator at cryogenic temperature:** Measured mechanical loss ($1/Q_{\mathrm{m}}$) of the 65th longitudinal mode of the quartz BAW resonator is indicated by black dots. Two-level system (TLS) loss is indicated by the blue line and Landau-Rumer (LR) loss is indicated by the green line. Between 5 and 10 K, the loss follows the temperature power scaling $T^{6.5}$. At lower temperature, TLS loss for quartz is expected to follow a $T^{0.3}$ trend. The sum of TLS and LR losses is shown by the orange curve, and extrapolation of the temperature to 1 K indicates that $T/Q_{\mathrm{m}} = 6.5 \times 10^{-11}$ K may be possible.

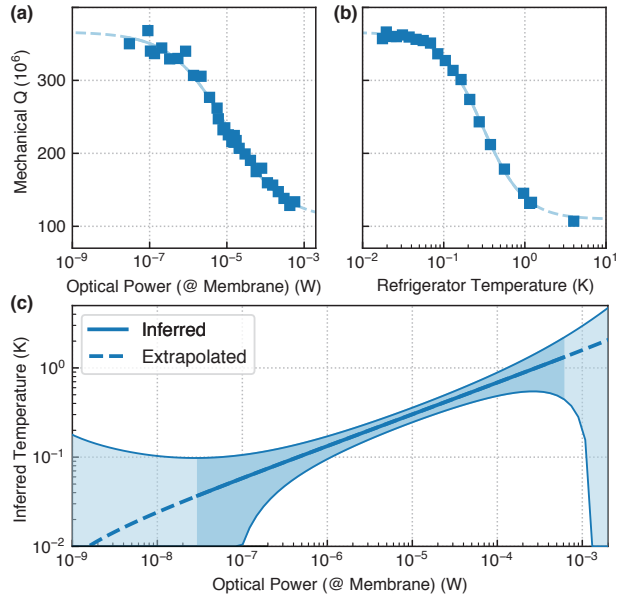

FIG. S2. **Low-temperature mechanical properties of a phononically shielded silicon nitride membrane resonator under optical illumination:** (a) Mechanical quality factor vs optical power traversing the membrane held at a refrigerator temperature of 15 mK. (b) Mechanical quality factor (probed with low optical power) vs refrigerator temperature. (c) Taking the mechanical quality factor as a proxy for the membrane temperature, we infer the effect of absorption heating. To this end, the generic polynomial model shown as line in panel (b) is inverted, and applied to the quality factors shown in panel (a).

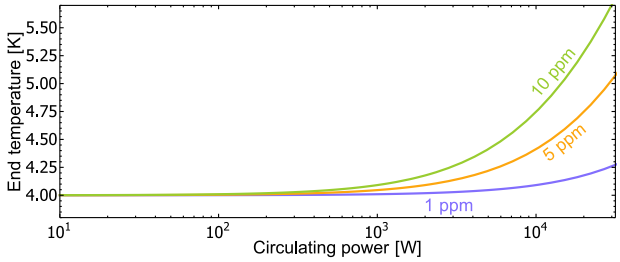

FIG. S3. **One-dimensional estimate of equilibrium temperature of the quartz bulk acoustic wave (BAW) resonator in the negative dispersion filter:** Various levels of optical absorption are shown, though single-crystal quartz BAW resonators can be reasonably expected to have less than 1 ppm absorption of 1064 nm light. The contacts to the BAW resonator are maintained at 4 K. Even at the high powers required to achieve white light signal recycling, a first estimate indicates that maintaining the resonator at cryogenic temperature is plausible.

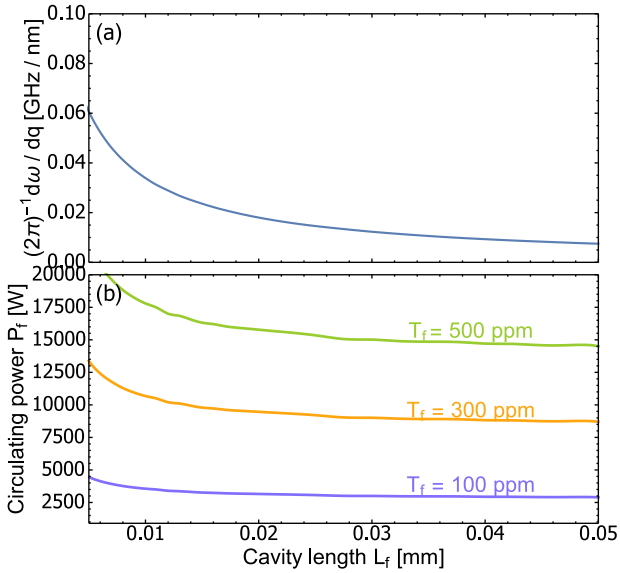

FIG. S4. **Optomechanical coupling requirement for white light signal recycling (WLSR) with bulk acoustic wave resonator:** The optomechanical coupling curves are calculated using a resonator with initial thickness $q_0 = 1$ mm and crystal center position x_p located at the midpoint of the optical cavity. (a) - Dependence of maximum optomechanical frequency shift $d\omega/dq$ on filter cavity length. (b) - Circulating power P_f required to achieve optomechanical anti-damping $\gamma_{opt}/(2\pi) = 900$ Hz versus filter cavity length L_f, for different values of filter input transmission T_f. This prescription is used for a WLSR configuration that produces somewhat lower bandwidth enhancement but also requires a factor of 13 less power versus the optimal WLSR described by equation 3 of the main text.

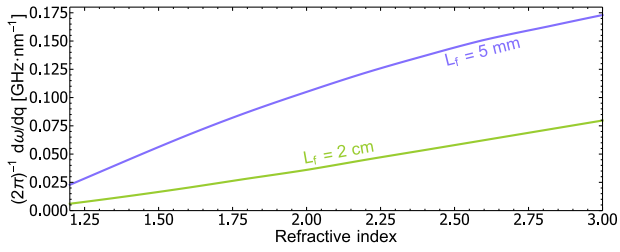

FIG. S5. **Bulk acoustic wave resonator optomechanical coupling versus refractive index**:The optomechanical frequency shift $d\omega/dq$ is calculated using the system described in main text Methods. Two different filter cavity lengths are shown - optomechanical coupling is smaller for longer cavities.

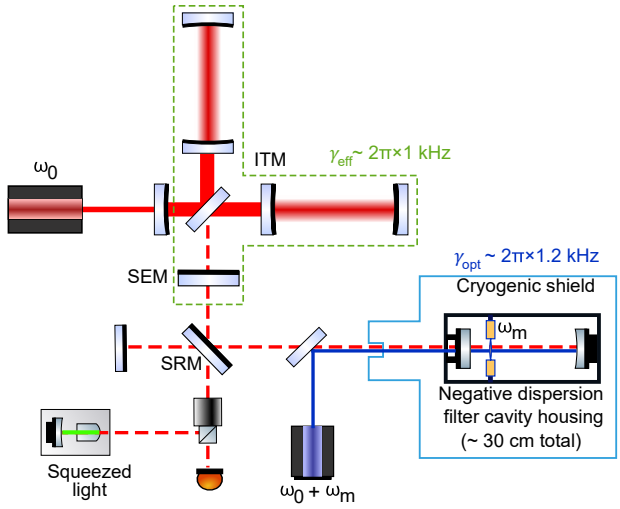

FIG. S6. **Alternate white light signal recycling configuration requiring less filter cavity pumping power:** The interferometer is dual recycled, operating in resonant sideband extraction mode. The interferometer output, filter cavity and photodetector are coupled via the signal recycling mirror (SRM). Unlike figure 1 of the main text, the signal extraction mirror (SEM) is not perfectly impedance matched to the input test mass (ITM). With respect to gravitational wave signals emerging out to the dark port, the interferometer can be considered as a two mirror cavity with effective bandwidth $\gamma_{\rm eff}/(2\pi) = 1$ kHz. The optomechanical anti-damping $\gamma_{\rm opt}$ is considerably lower than for the configuration shown in figure 1 of the main text.

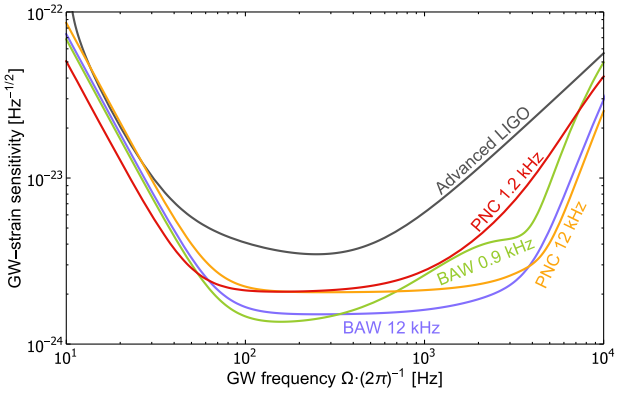

FIG. S7. **Comparison of white light signal recycling (WLSR) with different values of optomechanical anti-damping:** Different WLSR schemes are denoted by PNC for the phononic crystal resonator, BAW for the bulk acoustic wave resonator and the optomechanical anti-damping $\gamma_{\rm opt}/2\pi$ is also specified. The schemes denoted by "12 kHz" use the layout shown in figure 1 of the main text, while the other WLSR schemes use the layout shown in figure S6. We also note that the WLSR schemes here use 800 kW arm cavity circulating power and no application of frequency dependent squeezing. Input parameters are given in table S2. "Advanced LIGO" denotes the nominal design sensitivity shown in [27] at 800 kW arm cavity power.

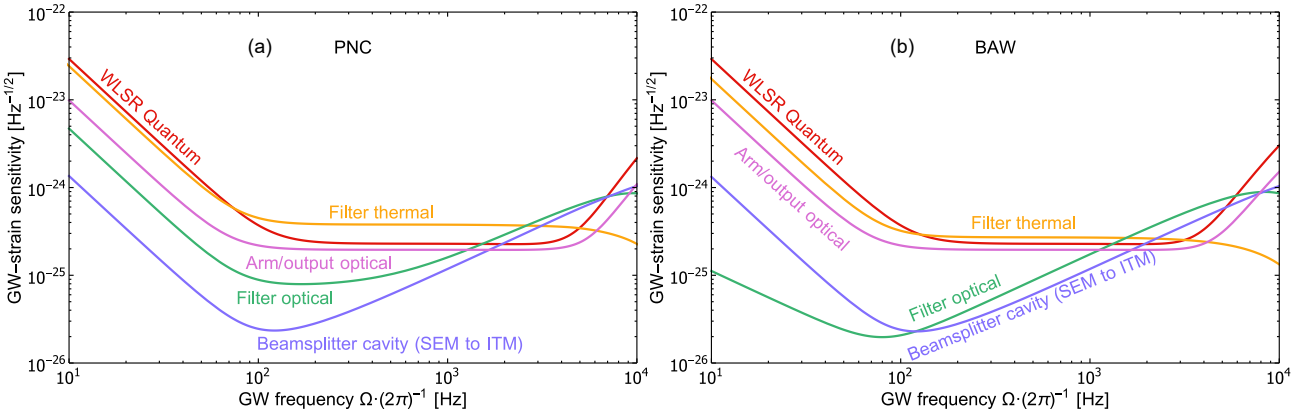

FIG. S8. **Noise budget of select white light signal recycling (WLSR) interferometers from the main text**: Breakdown of noise sources for WLSR interferometer using (a) phononic crystal resonator at 1 K, and (b) bulk acoustic wave resonator at 4 K, where the totals add up to the corresponding curves of figure 1 of the main text. Input parameters are given in table S1. The different noise sources are as follows: **WLSR Quantum:** (Red) Vacuum noise at the gravitational wave sideband frequency Ω, referred to the output of the detector. 10 dB frequency dependent quantum noise squeezing is applied in both of these plots. **Filter thermal:** (Orange) Thermal noise introduced by the mechanical resonator inside the filter cavity. **Filter optical:** (Green) Optical loss introduced inside the filter cavity. **Beamsplitter cavity:** (Blue) Power dependent optical losses that occur inside the beamsplitter cavity of the interferometer due to wavefront distortion. **Arm/output optical:** (Violet) Sum of power independent optical losses that occur in the interferometer arm cavity, signal recycling cavity and throughout the output train of the detector's optics.

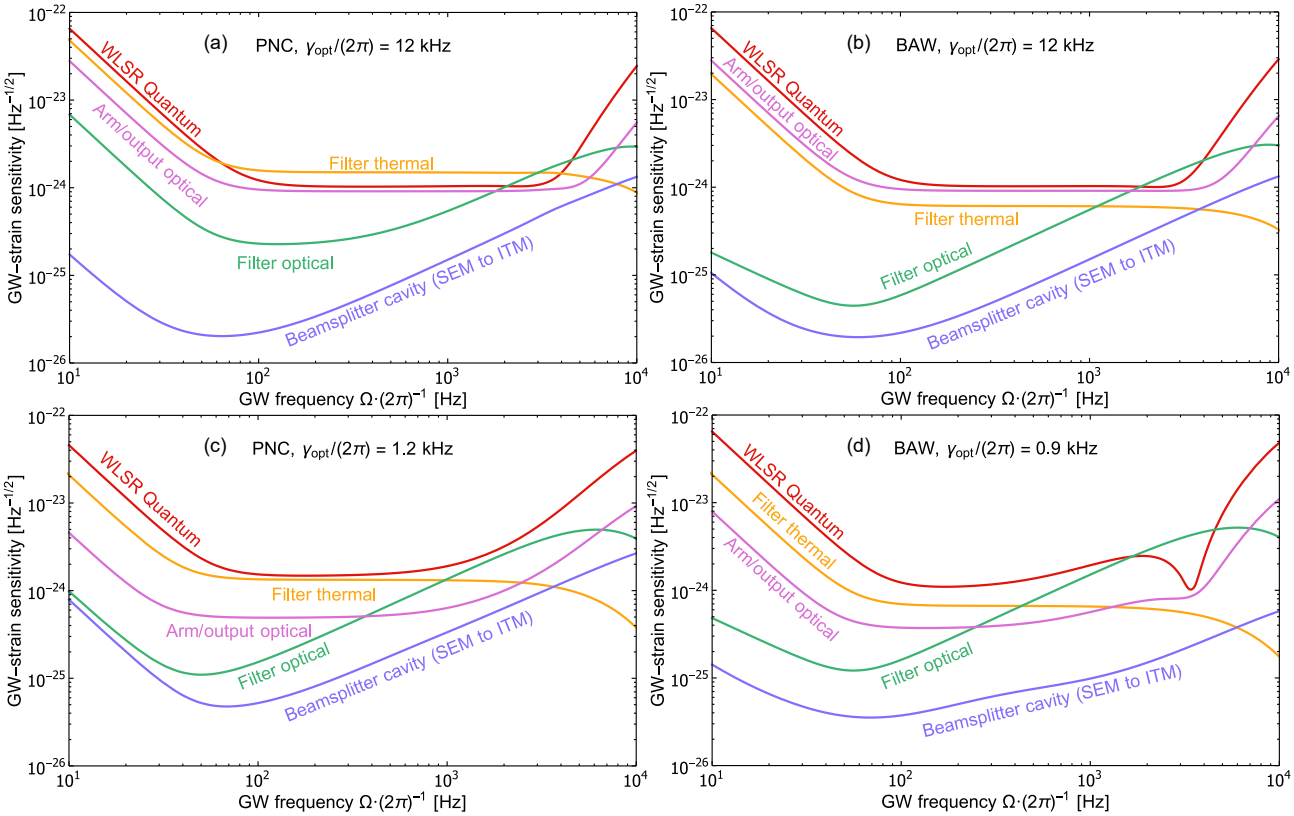

FIG. S9. **Noise budget of select white light signal recycling (WLSR) interferometers from Supplementary Notes**: Breakdown of noise sources for WLSR interferometers, with totals adding up to the corresponding curves of figure S7. The configuration shown in figure 1 of the main text is used to produce (a) with the phononic crystal resonator at 3 K, and (b) with the bulk acoustic wave resonator at 4 K. The configuration shown in figure S7 is used to produce (c) with the phononic crystal resonator at 3 K, and (d) with the bulk acoustic wave resonator at 4 K. The level of optomechanical anti-damping γ_{opt} is indicated in each plot. Input parameters are given in table S2. The different noise sources are as follows: **WLSR Quantum:** (Red) Vacuum noise at the gravitational wave sideband frequency Ω, referred to the output of the detector. No quantum noise squeezing is applied in any of these plots. **Filter thermal:** (Orange) Thermal noise introduced by the mechanical resonator inside the filter cavity. **Filter optical:** (Green) Optical loss introduced inside the filter cavity. **Beamsplitter cavity:** (Blue) Power dependent optical losses that occur inside the beamsplitter cavity of the interferometer due to wavefront distortion. **Arm/output optical:** (Violet) Sum of power independent optical losses that occur in the interferometer arm cavity, signal recycling cavity and throughout the output train of the detector's optics.

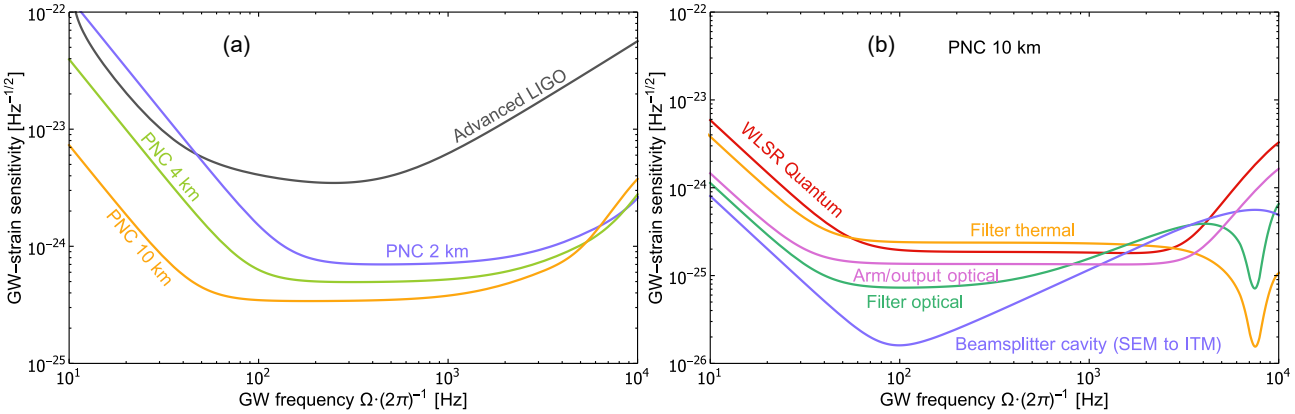

FIG. S10. **Change of white light signal recycling (WLSR) effect with interferometer arm lengths:** (a) These WLSR curves use the phononic crystal (PNC) resonator, configurations based on figure 1 of the main text and are calculated using loss parameters shown in table S1. The 4 km curve is identical to the curve labelled "PNC" in figure 1 of the main text. All WLSR curves operate at 4 MW arm cavity circulating power and use 10 dB frequency dependent squeezing. "Advanced LIGO" denotes the nominal design sensitivity shown in [27] at 800 kW arm cavity power. (b) Breakdown of noise sources for the 10 km WLSR interferometer using the PNC resonator, where the noise sources are as described in figures S8. Even with increased optical losses in the 1–5 kHz band as per table S1, the 10 km case still maintains superior gain/bandwidth product for frequencies relevant to neutron star detection.

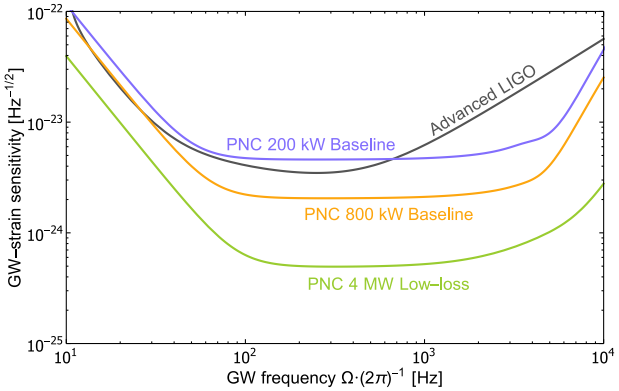

FIG. S11. **White light signal recycling (WLSR) effect at different levels of arm cavity power:** Comparison of WLSR across different interferometer arm powers, where "PNC 200 kW Baseline" uses parameters in the "PNC 200 kW" column of table S2, "PNC 800 kW Baseline" uses parameters in the "PNC 12 kHz" column of table S2 and "4 MW Low-loss" is identical to the PNC curve shown in figure 1 of the main text. "Advanced LIGO" denotes the nominal design sensitivity shown in [27] at 800 kW arm cavity power.